



Towards the quantized anomalous Hall effect in AlO_x-capped MnBi₂Te₄

Received: 30 May 2024

Accepted: 7 February 2025

Published online: 18 February 2025

Check for updates

Yongqian Wang^{1,2,9}, Bohan Fu^{1,2,9}, Yongchao Wang^{①,3}, Zichen Lian³, Shuai Yang^{1,2}, Yaxin Li^{②,3}, Liangcai Xu^{②,3}, Zhiting Gao⁴, Xiaotian Yang⁵, Wenbo Wang^{③,5}, Wanjun Jiang^{②,3,6}, Jinsong Zhang^{②,3,6,7}, Yanyu Wang^{②,3,6,7,8} & Chang Liu^{①,2,✉}

The quantum anomalous Hall effect in layered antiferromagnet MnBi₂Te₄ harbors a rich interplay between magnetism and topology, holding a significant promise for low-power electronic devices and topological anti-ferromagnetic spintronics. In recent years, MnBi₂Te₄ has garnered considerable attention as the only known material to exhibit the anti-ferromagnetic quantum anomalous Hall effect. However, this field faces significant challenges as the quantization at zero magnetic field depending critically on fabricating high-quality devices. In this article, we introduce a straightforward yet effective method to mitigate the detrimental effect of the standard fabrication on MnBi₂Te₄ by depositing an AlO_x layer on the surface before fabrication. Optical contrast and magnetotransport measurements on over 50 MnBi₂Te₄ demonstrate that AlO_x can effectively preserve the pristine states of the devices. Surprisingly, we find this simple method can significantly enhance the anomalous Hall effect towards quantization, which resolves a longstanding challenge in the field of MnBi₂Te₄. Scaling relation analysis further reveals the intrinsic mechanism of anomalous Hall effect dominated by Berry curvature at various magnetic configuration. By tuning the gate voltage, we uncover a gate independent magnetism in odd-layer MnBi₂Te₄ devices. Our experiments not only pave the way for the fabrication of high-quality dissipationless transport devices, but also advance the investigation of exotic topological quantum phenomena in 2D materials.

Magnetic topological materials have emerged as a frontier in condensed matter physics, providing promising platforms for exploring exotic quantum phenomena and applications in topological spintronics^{1–3}. For uncovering novel topological physics, successful fabrication of high-quality devices with quantized transport is

prerequisite. As the first identified material possessing van der Waals characteristics, intrinsic magnetism, and nontrivial band topology simultaneously, MnBi₂Te₄ not only exhibits rich novel quantized phenomena when exfoliated down to few-layer limit^{4–6}, but is also considered capable of addressing the disorder issue that is prevalent in

¹School of Physics, Renmin University of China, Beijing, China. ²Key Laboratory of Quantum State Construction and Manipulation (Ministry of Education), Renmin University of China, Beijing, China. ³State Key Laboratory of Low Dimensional Quantum Physics, Department of Physics, Tsinghua University, Beijing, China. ⁴Beijing Academy of Quantum Information Sciences, Beijing, China. ⁵School of Physical Science and Technology, ShanghaiTech Laboratory for Topological Physics, ShanghaiTech University, Shanghai, China. ⁶Frontier Science Center for Quantum Information, Beijing, China. ⁷Hefei National Laboratory, Hefei, China. ⁸New Cornerstone Science Laboratory, Frontier Science Center for Quantum Information, Beijing, P. R. China. ⁹These authors contributed equally: Yongqian Wang, Bohan Fu. ✉ e-mail: liuchang_phy@ruc.edu.cn

magnetically doped topological insulators (TIs)⁷. The bulk crystal of MnBi₂Te₄ can be regarded as a stacking of Te-Bi-Te-Mn-Te-Bi-Te septuple layer (SL) along z-direction (Fig. 1a). A-type antiferromagnetic (AFM) structure with interlayer AFM order and intralayer ferromagnetic (FM) order forms below the Néel temperature (T_N) ~ 25 K. When interacting with band topology, this layer-dependent magnetic ordering can give rise to a rich variety of topological quantum states and exotic magnetoelectric response^{8–15}. In odd-SL MnBi₂Te₄ film, the gapped Dirac topological surface states due to the parallel surface magnetizations drive the system into the quantum anomalous Hall (QAH) state with 1D dissipationless chiral edge state transport⁸ (Fig. 1b). This manifests as a quantized Hall conductivity $\sigma_{xy} = Ce^2/h$ at zero-magnetic field ($\mu_0H = 0$), where C represents the Chern number, e is the electron charge, and h is the Planck constant. In even-SL MnBi₂Te₄, the opposite surface magnetizations result in vanishing σ_{xy} and lead to the axion insulator state characterized by a zero plateau at μ_0H (ref. 10). Recent progresses in MnBi₂Te₄ have unveiled a plethora of novel topological phenomena, including the Möbius insulator¹⁶, layer Hall effect¹¹, axion optical induction¹⁷, and quantum metric non-linear transport^{18,19}.

Although the QAH effect and axion insulator states have been observed in 5- and 6-SL MnBi₂Te₄, the temperature (T) below which quantization is realized remains much lower than its T_N . A more formidable challenge arises from the exceptionally low yield of MnBi₂Te₄ film exhibiting quantized transport. Over the past five years, neither perfectly quantized^{9,12,13,15,20–22} nor zero plateau^{12,17–19,22} at $\mu_0H = 0$ can be

consistently reproduced. The lack of quantization not only obstructs the discovery of new phenomena but also complicates the interpretation of available data. Possible reasons include various structural defects or impurity phases^{23–27}, instability of surface electronic structures^{28–31}, and weakened surface out-of-plane magnetic anisotropy (MA)^{31–33}. Our recent studies combining optical contrast (O_c), transport, magneto-optical Kerr effect (MOKE) measurements revealed a substantial impact of fabrication on the properties of MnBi₂Te₄ devices²². The contact with photoresist not only reduces the O_c value during the fabrication process, but may also results in mismatched even-odd-layer-dependent magnetotransport²². The mechanism likely originates from the formation of a dead insulating layer on the MnBi₂Te₄ surface, which is caused by the change of surface band structure^{30,34,35}. Over the past five years, developing a low-damage fabrication method to reproduce the QAH effect has become one of the most pressing tasks in the field of magnetic topological quantum materials and devices.

In this work, we optimize the fabrication process by depositing an AlO_x protective layer on MnBi₂Te₄ top surface prior to the standard electron beam lithography (EBL). To ensure a good ohmic contact between the MnBi₂Te₄ and electrode, we implement an additional Ar ion etching step to selectively remove the AlO_x at the electrode areas after the lithography process. By employing this method, we can fabricate transport devices with good electrical contact while using an insulating AlO_x layer to fully isolate the photoresist Polymethyl Methacrylate (PMMA). Through optical measurement on a series of

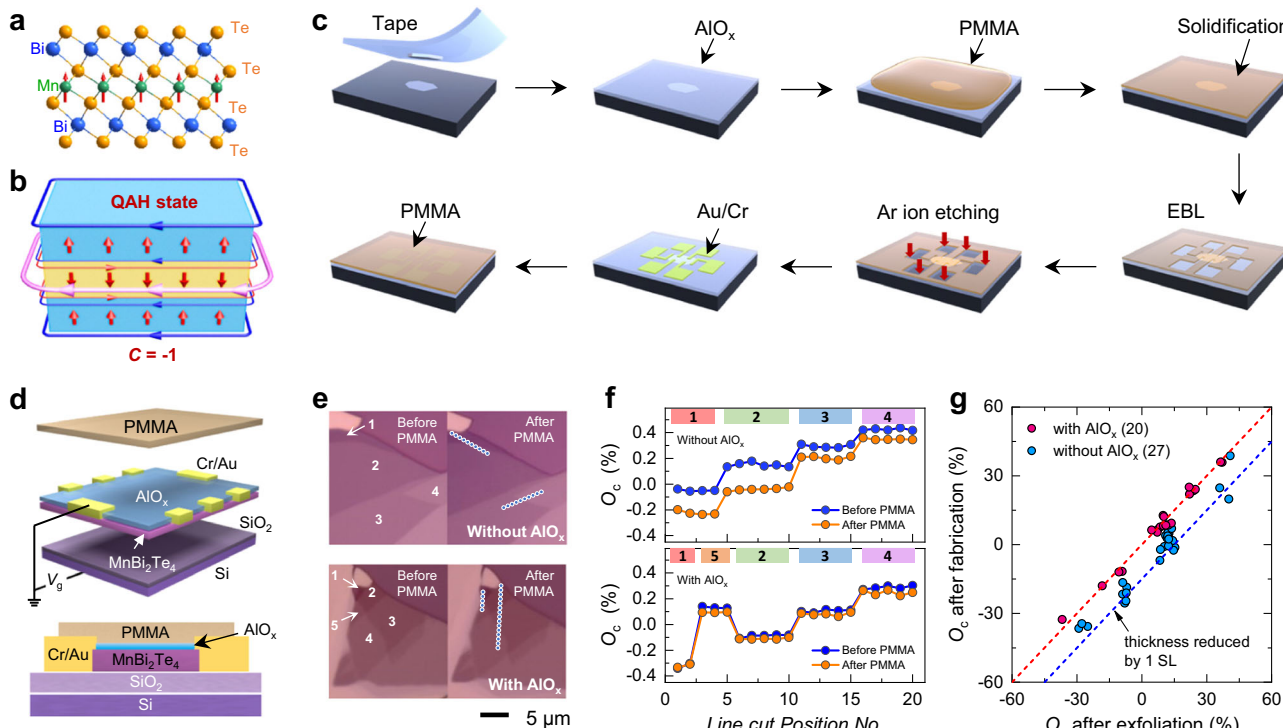


Fig. 1 | Fabrication and optical contrast characterizations of few-layer MnBi₂Te₄ flakes. **a** Crystal structure of MnBi₂Te₄. **b** Schematic of the QAH effect in an odd-SL MnBi₂Te₄. The red arrows in **a** and **b** represent the magnetic moments of Mn in each layer. **c** Illustration of the device fabrication process. This method is developed based on the standard EBL process. By simply depositing a thin layer of AlO_x on the MnBi₂Te₄ surface, the PMMA resist is isolated from the top surface. The high insulation and compactness of AlO_x make it possible to fabricate Hall bar patterns while protecting the sample from chemical reagents. **d** Front and side views of a transport device. **e** Optical images of MnBi₂Te₄ flakes exfoliated from the same crystal. The top (bottom) panel compares the color change of MnBi₂Te₄ flakes without (with) AlO_x capping before and after contact with PMMA, respectively.

f Variation of O_c for selected spots along the line traces in flakes of different thicknesses in **e**. O_c is defined as $(I_{\text{flake}} - I_{\text{substrate}})/I_{\text{substrate}}$, where I_{flake} and $I_{\text{substrate}}$ are the intensity of MnBi₂Te₄ and substrate, respectively. **g** Statistical analysis of O_c of 47 MnBi₂Te₄ flakes with (red) and without (blue) AlO_x capping layer. Different data points represent the O_c of different flakes after mechanical exfoliation and after contact with PMMA, respectively. The red and blue dashed line denote the O_c reduction by 0 and 20%, respectively, corresponding to no change and a decrease of effective thickness by one layer. The variability of the degree of O_c reduction among different flakes does not stem from measurement errors but rather arises from the inhomogeneities and sample quality fluctuations within the bulk crystal.

MnBi_2Te_4 thin flakes, we find that the fabrication issue induced by PMMA photoresist is largely mitigated. Most importantly, this simple idea overcomes the bottlenecks in the field of topological quantum materials over the past five years. We not only achieve the QAH effect in multiple MnBi_2Te_4 devices, but also reveal the key factors influencing the zero-magnetic-field quantization. Our work introduces a simple yet effective method for fabricating high-quality transport devices, paving the way for realizing the QAH effect and exploring more exotic topological quantum phenomena.

Results

Device fabrication and optical contrast

We got inspiration from previous experiments where those MnBi_2Te_4 devices exhibiting large anomalous Hall (AH) effect often had Al_2O_3 on the bottom of the flakes^{8,21,36}, either as a substrate or a supporting layer. This implies that the contact with Al_2O_3 may help to improve the quality of MnBi_2Te_4 device. Combined with our recent finding of the detrimental effect of fabrication on the top surface of MnBi_2Te_4 , we come up with a straightforward yet effective idea that by depositing an AlO_x layer on top of MnBi_2Te_4 to achieve the QAH effect. Figure 1c shows the schematic of the fabrication process. First, we transferred thick MnBi_2Te_4 flakes from a bulk crystal to the substrate using a Scotch tape. We then employed the mechanical exfoliation method to obtain the flakes with target thickness. The one-to-one correspondence between O_c and thickness allows the rapid determination of SL number by optical method¹¹. Subsequently, a 3-nm AlO_x layer was deposited by thermal evaporation. We then adopted the standard EBL process to expose the designed Hall bar patterns. Next, the AlO_x layer above the designed electrode areas was etched away by Ar ion etching, followed by the deposition of Cr/Au electrodes. To ensure the charge transport is not affected by the etching process in the contact region, we assessed the MnBi_2Te_4 thickness in the etched region by O_c and atomic force microscopy measurements (see Supplementary Figs. 1 and 2). Finally, a PMMA layer was coated for further protection. The details of the fabrication are described in the Methods section. Compared to the Al_2O_3 -assisted exfoliation and stencil mask method⁸, our method is more straightforward and is based on the standard EBL process, which enables the fabrication of specific nano-devices with reduced sample size. Furthermore, since the AlO_x is on the top surface, it not only offers an effective protection, but also can be used as a dielectric layer for top gate controllability.

Figure 1d depicts a schematic of a Hall bar device covered with AlO_x capping layer and its cross-sectional view. To investigate the influence of AlO_x on MnBi_2Te_4 , we first compare the optical properties of MnBi_2Te_4 flakes with varied thicknesses, which were exfoliated from the same single crystal (Supplementary Fig. 3 for the O_c change in each step). The optical images in Fig. 1e clearly suggest that for flakes without AlO_x (up panel), the colors of all four regions change significantly before and after contact with PMMA. In contrast, those regimes with AlO_x (down panel) do not exhibit noticeable change during the same process. To further explore the effect of AlO_x quantitatively, we extract their O_c values of the selected spots along the line traces in Fig. 1e and compare their variations directly. As shown in Fig. 1f, significant reductions of O_c in all the four areas without AlO_x are observed. In contrast, O_c remains nearly unchanged for the five areas with AlO_x capping layers. To eliminate the influences of device quality fluctuations on our observation, we compare the O_c values of 47 MnBi_2Te_4 exfoliated from the same crystal (Fig. 1g). Different data points represent the O_c of different flakes after exfoliation and after contact with PMMA. The distribution of O_c falls well into two parts (red and blue dots). According to the one-to-one correspondence between O_c and thickness¹¹, the decrease of O_c indicates the reduction of effective thickness during fabrication. The red and blue dashed lines represent the O_c reduction by 0 and 20 %, respectively, which corresponds to unchanged thickness and a decrease of thickness by one SL.

For the flakes without AlO_x layer, regardless of their initial O_c values, most of the samples display a pronounced decrease in O_c after fabrication. Notably, the degree of O_c change exhibits certain variability among different samples. This behavior does not stem from measurement errors but rather originates from the inhomogeneities and sample quality fluctuations within the MnBi_2Te_4 crystal. Such sample-dependent sensitivity to fabrication has also been observed in previous experiments²². These results clearly demonstrate that AlO_x can effectively mitigate the damages caused by PMMA²².

Statistical analysis of the influence of AlO_x on transport properties

In magnetic topological systems, the AH effect typically results from three mechanisms: intrinsic Berry curvature $\Omega(\mathbf{k})$, skew-scattering, and side-jump. In the transport of MnBi_2Te_4 , due to defects or impurity phases, all the three mechanisms could contribute to the AH effect²⁰. However, in an ideal quantized Hall system, the transverse transport should be dominated by $\Omega(\mathbf{k})$ in momentum (\mathbf{k}) space³⁷. Theoretically, σ_{xy} can be calculated by integrating Ω over \mathbf{k} , as expressed by:

$$\sigma_{xy} = -\frac{e^2}{2\pi\hbar} \int \Omega(\mathbf{k}) d^2\mathbf{k}$$

When the Fermi level (E_F) is tuned into the magnetic exchange gap, the integral of Ω equals the C number multiplied by 2π , resulting in the quantization of σ_{xy} at e^2/h . To investigate the influence of AlO_x on the intrinsic AH effect, we measured the transport properties of 17 odd-SL MnBi_2Te_4 devices. All the data shown in the main text was obtained at the charge neutral point (CNP) unless otherwise specified. Prior to this, we measured the current–voltage curve of the AlO_x layer to exclude its contribution to transport (Supplementary Fig. 4). Figure 2a–d shows the μ_0H dependence of σ_{xy} and σ_{xx} for two 7-SL devices exfoliated from the same thick flake on the same tape. Both devices show quantized σ_{xy} at the high μ_0H Chern insulator state ($C = -1$). However, their AH effects at zero field exhibit dramatically different behaviors. For device #1 without AlO_x (Fig. 2a), σ_{xy} almost vanishes at the low μ_0H AFM regime. Such behavior is consistent with our previous observation that fabrication process can damage the top surface, leading to a reduction of effective thickness by one SL²². However, for the device #9 fabricated by the current method, a large σ_{xy} accompanied with a square-shaped hysteresis is observed. The insets show the schematic distribution of the topological surface states wave functions (green) for devices without and with AlO_x . To further demonstrate the influence of AlO_x on transport more clearly, we display the gate voltage (V_g) dependent σ_{xy} and σ_{xx} at $\mu_0H = -8$ T and 0 for the two devices, as displayed in Fig. 2b, d. For device #1, σ_{xy} smoothly crosses zero with increasing V_g , indicating a reduced gap size during the fabrication process²². In contrast, device #9 shows a wide plateau in σ_{xy} in the same V_g range of the Chern insulator, indicating an incipient QAH state in the AFM state.

For 2D materials, the transport properties of thin flakes are inevitably influenced by the fluctuations of device qualities. Previous experiments have suggested that MnBi_2Te_4 exhibits sample-dependent properties, even for flakes prepared from the same crystal^{8,24,25}. Therefore, it is challenging to expect any fabrication method to guarantee the production of perfect QAH devices with 100 % certainty. To demonstrate that the enhancement of the AH effect arises from AlO_x , we studied the transport properties of 17 odd-number-SL MnBi_2Te_4 devices, with the data presented in Fig. 2e, f. These devices were numbered based on the increasing order of their σ_{xy} at $\mu_0H = 0$. Apart from devices #2, #4, #6, and #8 that were acquired from crystal #1, all the other 13 devices were obtained from crystal #2. All the devices exhibit $\sigma_{xy} = e^2/h$ at the high μ_0H Chern insulator state, indicating the overall high quality of our devices. However, these devices show dramatically different behaviors in their AH effect.

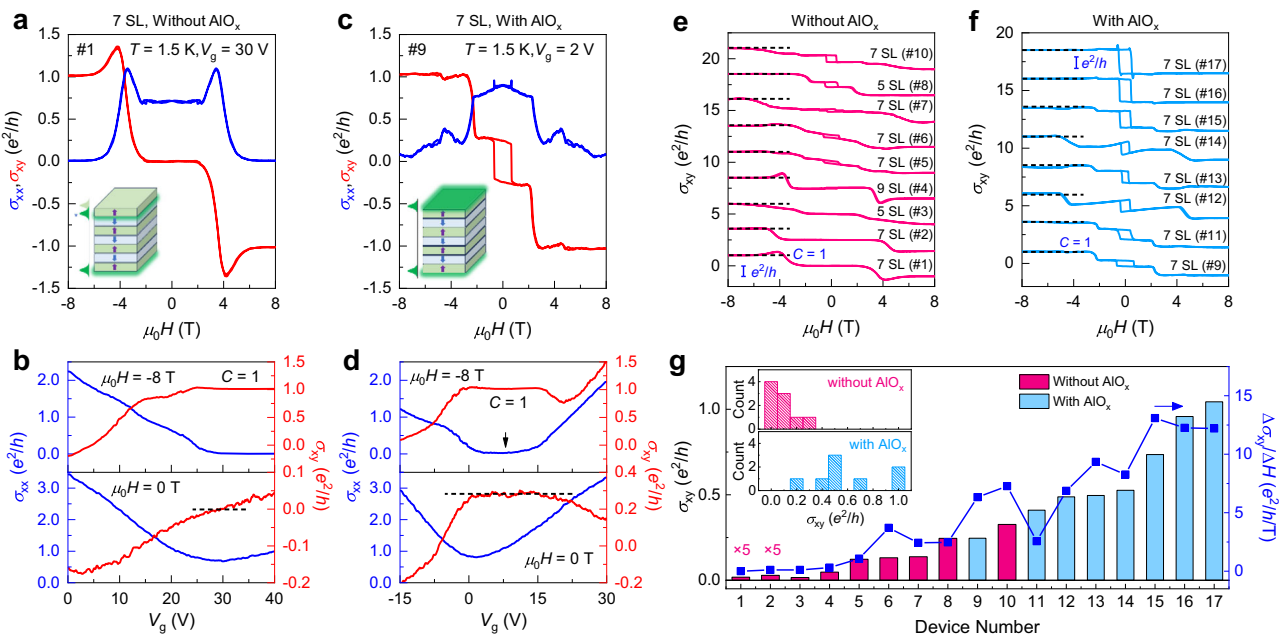


Fig. 2 | Comparison of transport behaviors for devices obtained by different fabrication methods. **a** Transport behaviors at CNP for a 7-SL device without AlO_x covering layer. Due to fabrication effects, the surface state shifts down to the second SL (inset), and the hysteresis of σ_{xy} near zero field almost disappears. **b** Variation of σ_{xy} and σ_{xx} as a function of V_g at $\mu_0 H = -8 \text{ T}$ and 0 T , respectively. The black dashed line represents the V_g window where σ_{xy} plateaus coexist under zero and high $\mu_0 H$ conditions, respectively. **c** Transport behavior of a 7-SL device exfoliated from a MnBi_2Te_4 flake on the same tape, but with an AlO_x layer deposited during the fabrication process. The large hysteresis indicates excellent protection of device performance. The inset illustrates that the topological surface state remains

predominantly distributed on the outermost surface due to the protection of AlO_x . **d** In the same V_g range of high field Chern insulator state (marked by black dashed line), σ_{xy} at $\mu_0 H = 0$ exhibits a broad plateau during sweeping V_g . **e, f** $\mu_0 H$ -dependent σ_{xy} at $T = 1.5 \text{ K}$ for 17 odd-SL devices. The only difference during their fabrication lies in whether the surface was deposited with AlO_x . All the devices exhibit quantized σ_{xy} at high $\mu_0 H$, as marked by the black dashed lines. **g** Summarized σ_{xy} at $\mu_0 H = 0$ and $\Delta\sigma_{xy}/\Delta H$ values at the plateau transition for the 17 devices. Devices with AlO_x capping layer (blue) generally show a larger AH effect than those without AlO_x (red). The inset displays the histograms of AH effect distribution of the 17 devices. The size of each bin on the σ_{xy} -axis is $0.1 \text{ } e^2/\text{h}$.

Remarkably, the 9 devices without AlO_x layer exhibit small σ_{xy} at $\mu_0 H = 0$. And some devices even exhibit almost indiscernible hysteresis. In sharp contrast, all the other 8 devices with AlO_x capping layer manifest large σ_{xy} and square-shaped hysteresis, with two devices almost quantized at e^2/h . Figure 2g summarizes the σ_{xy} at $\mu_0 H = 0$ of these devices. To largely avoid any artificial trend, we adopted the strategy in previous statistical studies of MnBi_2Te_4 crystals²⁵ by sorting the σ_{xy} from smallest to largest. In the inset of Fig. 2g, we also present the histograms of their σ_{xy} distribution. The size of each bin on the σ_{xy} -axis is $0.1 \text{ } e^2/\text{h}$. For the devices without AlO_x , their σ_{xy} values are distributed within the range of 0 to $0.3 \text{ } e^2/\text{h}$. In contrast, for those devices with AlO_x , their σ_{xy} distribution displays a clear shift towards higher values. Notably, despite not all devices with AlO_x exhibit the QAH effect, their AH effects have already surpassed the values for most MnBi_2Te_4 devices in literatures^{9,11–13,20,22}. In Fig. 2g, we also summarized the values of $\Delta\sigma_{xy}/\Delta H$ of the 17 devices (blue points), which represent the sharpness of magnetic transition. The variation of $\Delta\sigma_{xy}/\Delta H$ aligns with the trend of σ_{xy} . These results undoubtedly demonstrate that AlO_x plays a significant role in enhancing the AH effect.

The fabrication of high-quality devices enables us to compare the influences of magnetic properties on transport. Figure 3a–c shows the $\mu_0 H$ -dependent σ_{xx} and σ_{xy} for three devices obtained from the same crystal. Fortunately, for devices #11 and #16, they were obtained on the same substrate during one cleaving process. It enables us to further explore the influences of AlO_x on MnBi_2Te_4 flake while preserving the consistency of the devices. Overall, the three devices manifest consistent transport behaviors, with their main differences being the values of σ_{xx} and σ_{xy} at $\mu_0 H = 0$. However, the sharpness of the plateau transition, which reflects the magnetic flipping process, differs dramatically. For device #11, the σ_{xy} and σ_{xx} at $\mu_0 H = 0$ are 0.5 and $1.1 \text{ } e^2/\text{h}$, respectively, and the transition is relatively gentle. For

device #16, although the value of σ_{xx} does not change, σ_{xy} is significantly improved to $0.96 \text{ } e^2/\text{h}$, comparable to the value in previous report⁸. In addition, the plateau transition is also sharper than that of device #11. Device #17 completely enters the QAH state, with σ_{xy} reaching e^2/h and σ_{xx} dropping to 0. Because the QAH effect in magnetic TIs originates from the exchange field between local moments and electron spins³⁸. The out-of-plane magnetic order plays a crucial role in the $\mu_0 H$ -dependent transport behaviors. Therefore, the improved quantization along with the sharp σ_{xy} transition suggests that device #17 is likely to have a stronger out-of-plane MA.

The scaling relation between σ_{xy} and σ_{xx} may further help us understand the role of AlO_x in enhancing the QAH effect. Figure 3d–f displays the variation of σ_{xy} as a function of σ_{xx} during the cooling process under different $\mu_0 H$ and V_g s. As the AFM order strengthens at low T s, σ_{xy} begins to exhibit behavior independent of σ_{xx} and gradually approaches quantization, which is of typical the scaling behavior of the intrinsic AH effect dominated by $\Omega(\mathbf{k})$ (ref. 37). Upon increasing $\mu_0 H$, the device undergoes AFM, canted AFM, and finally enters FM state, accompanied by σ_{xy} saturating at e^2/h at higher T s. For device #11 with relatively weaker out-of-plane magnetic order, the exchange gap is expected to be smaller in the AFM state, thermal fluctuations could more easily smear out the role of $\Omega(\mathbf{k})$ (top in Fig. 3g). Therefore, complete quantization appears only when all moments are parallelly aligned because the gap is overall positively correlated with magnetization. However, for the device #17 with stronger out-of-plane order, the larger gap allows for σ_{xy} reaching quantization even in the AFM state despite a small net moment. The influence of different magnetic configurations on exchange gap and $\Omega(\mathbf{k})$ is illustrated in Fig. 3g. $\Omega(\mathbf{k})$ can be interpreted as an effective $\mu_0 H$ in \mathbf{k} space acting on electrons. The red and blue represent the distribution of $\Omega(\mathbf{k})$ of opposite sign in conduction and valence band, respectively.

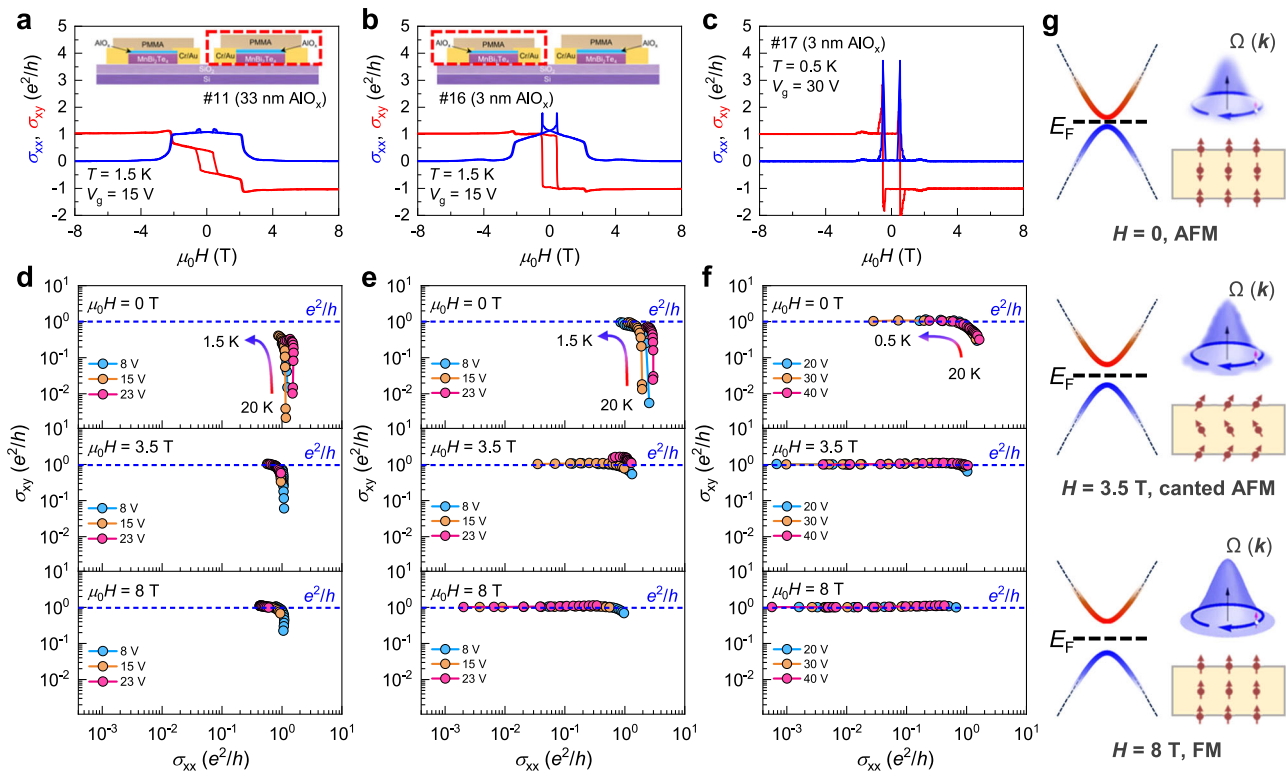


Fig. 3 | Scaling relation between σ_{xy} and σ_{xx} of the intrinsic AH effect. **a–c** $\mu_0 H$ -dependent σ_{xy} and σ_{xx} for three 7-SL devices exfoliated from the same crystal. Devices #11 and #16 were obtained simultaneously in one cleaving process on the same substrate, with the former one undergoing an extra AlO_x deposition process, having a thickness of 33 nm. **d–f** Evolution of σ_{xy} with σ_{xx} during the cooling process. With the formation of AFM order as lowering T_s , the scaling relation between σ_{xy} and σ_{xx} at different V_g s gradually collapses into one single curve, and σ_{xy}

saturates at e^2/h . The σ_{xx} independent behavior reflects the typical Berry curvature-dominated mechanism of the AH effect. **g** Schematics of the distribution of Berry curvature. From top to bottom, as the AFM order is tuned to the FM order, the out-of-plane component of the total magnetization is enhanced. As a result, the exchange gap increases, and the Berry curvature exhibits greater robustness against thermal fluctuations.

Gate voltage-independent magnetism

Next, we investigate the influence of V_g on the magnetic properties of MnBi_2Te_4 devices. Previous studies have revealed different V_g -dependent magnetism on magnetically doped TIs^{39–41}. The electrical control of van der Waals magnetism has also attracted wide attention. As the first layered topological antiferromagnet, it remains unclear whether V_g can exert similar effects. Figure 4a, b displays the $\mu_0 H$ -dependent σ_{xy} and σ_{xx} for device #16 at various T_s . The hysteresis vanishes at around $T = 21 \text{ K}$, accompanied by the disappearance of σ_{xx} peaks. To quantitatively investigate the changes in the AFM state, we extract the coercive field (H_c) values at different V_g s and plot them as a function of T with an offset of 0.25 T (Fig. 4c). The H_c dependence of T can be well described by the power law $-(1 - T/T_N)^\beta$, where β represents the critical exponent. We notice that V_g has almost negligible effect on the AFM order. T_N remains a constant at -21.3 K and β maintains at -0.52 . Similar results were also observed in previous neutron diffraction on MnBi_2Te_4 bulk crystal and reflectance magneto-circular dichroism (RMCD) measurement on exfoliated thin flakes^{14,42}. Our experiments further point that this critical behavior cannot be tuned by a bottom V_g . Figure 4e shows the colormap of σ_{xy} as a function of V_g and $\mu_0 H$. It clearly shows that H_c is independent of V_g , further supporting the V_g -independent magnetism in odd-SL MnBi_2Te_4 device. Reproducible results obtained from another two 7-SL MnBi_2Te_4 with and without AlO_x capping layer are documented in Supplementary Figs. 5 and 6.

Discussion

Finally, we discuss the possible mechanisms underlying the enhancement of AH effect. In our previous research, we found that the coating of PMMA during the EBL process reduces the O_c of MnBi_2Te_4 , leading

to a reduction of effective thickness²². AlO_x serves as an effective barrier by isolating the surface from direct contact with the resist, thus providing a substantial protection for MnBi_2Te_4 . However, in the history of 2D materials, the most widely used and effective capping layer for protection is $h\text{-BN}$, rather than AlO_x . In fact, previous experiments have suggested that the oxidation process may alter the intrinsic properties of MnBi_2Te film²⁸, therefore, using an AlO_x capping layer to protect MnBi_2Te is unconventional (Supplementary Fig. 7 for the aging effect). Furthermore, beyond employing a protective layer, a shadow mask method can also be employed to avoid direct contact with PMMA resist. However, many experiments have demonstrated that even employing these methods^{13,18,20,21}, the AH effect remains non-quantized. Interestingly, a comparison of recent transport experiments in MnBi_2Te_4 reveals that regardless of the different device preparation or electrode deposition methods, all MnBi_2Te_4 devices exhibiting pronounced AH effect have one surface in contact with Al_2O_3 (refs. 8,21,36). In these experiments, Al_2O_3 is positioned under MnBi_2Te_4 and does not provide any protection to the top surface. Hence, the simple protective role is insufficient to explain the close correlation between large AH effect and AlO_x in current experiments. It naturally raises the question of whether AlO_x may play an additional role beyond protection.

Our scaling relation studies imply that the enhancement of perpendicular magnetic order may be crucial for the QAH effect. Based on our experimental data and the results in previous studies, we discuss the potential additional roles that AlO_x may play. A conceivable scenario is the electric field enhanced magnetism at the $\text{AlO}_x/\text{MnBi}_2\text{Te}_4$ interface^{43,44}. However, this scenario can be largely excluded because our V_g -dependent experiments demonstrate that V_g has a small

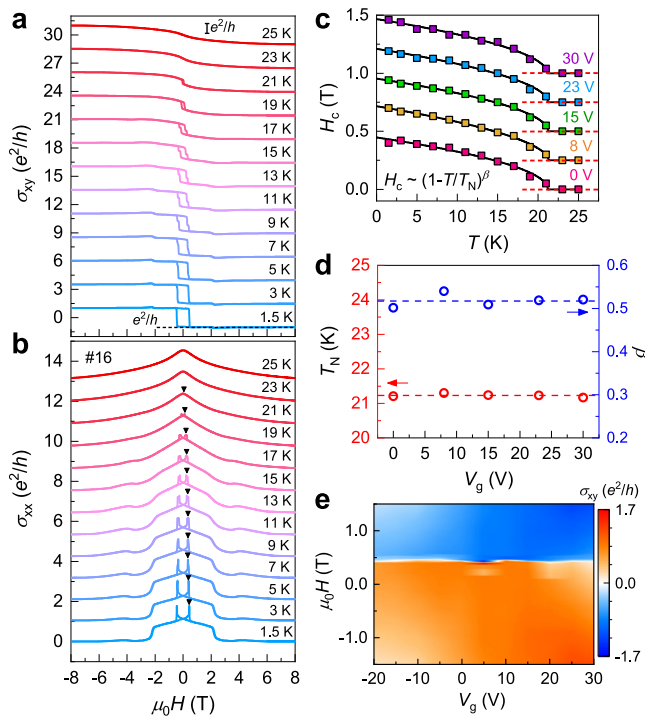


Fig. 4 | Transport and magnetic properties tuned by V_g . **a, b** $\mu_0 H$ -dependent σ_{xy} and σ_{xx} at the CNP for device #16 at various T s. The hysteresis and the double peak in σ_{xx} disappear at around $T = 21$ K. The black triangles mark the position of H_c at different T s. **c** H_c extracted from the field sweep data as a function of T at varied V_g s. The solid squares are the data points. The black lines are the data fittings in the form of $-(1 - T/T_N)^\beta$. The red dashed lines represent the position of $H_c = 0$ for each curve. **d** Summarized T_N and β from the fittings as a function of V_g . The blue and red dashed lines represent the average positions of the β and T_N values for different V_g s. T_N and β are found to be -21.2 K and 0.52 , respectively, both of which are independent of V_g . **e** Colormap of σ_{xy} in the parameter space of $\mu_0 H$ and V_g . The boundary between blue and orange region marks the V_g -independent H_c .

influence on magnetism. Another possible scenario is the enhanced perpendicular magnetic anisotropy (PMA) by AlO_x . In spintronics, many experiments have demonstrated that depositing amorphous oxide (such as AlO_x , MgO , TaO_x , HfO_x) can substantially increase the interfacial PMA at the interface between oxides and magnetic materials^{45–47}. Therefore, it is naturally expected that the AlO_x layer strengthens the interfacial PMA of MnBi_2Te_4 , which in turn enhances the AH effect. In fact, there has been theoretical calculations suggesting that the MA in monolayer MnBi_2Te_4 is weak due to the weak p - d hybridization between Mn and Te (ref. 48). Later, inelastic neutron scattering pointed that for MnBi_2Te_4 crystals, the MA is enhanced by the interlayer two-ion anisotropy³². However, due to the absence of neighboring layers, the MA of the surface is still weak. These results naturally explain why, in all current MnBi_2Te_4 experiments exhibiting a large AH effect, the device must have at least one surface in contact with AlO_x .

To validate our conjectures, we conducted cryogenic magnetic force microscopy (MFM) measurement to directly visualize the magnetic properties across different regions of the same 7-SL MnBi_2Te_4 . As anticipated, the region with AlO_x manifests a much stronger magnetic signal compared to the region without AlO_x (Supplementary Fig. 8). Moreover, to further explore the influence of AlO_x on QAH effect, we compared the magnetic hysteresis loops of two fully quantized devices with single-sided and double-sided AlO_x contacts. Interestingly, the device with both top and bottom surfaces in contact with AlO_x shows a larger H_c (see Supplementary Fig. 9 for details). In magnetic materials, H_c is proportional to the strength of PMA⁴⁹. The larger H_c in device with

double-sided AlO_x aligns with the finding that AlO_x can enhance the interfacial PMA^{45–47}. In addition to PMA, a recent calculation has also suggested that bringing MnBi_2Te_4 surface close to a polar insulator can modify the surface potential, which is helpful for the QAH effect³⁰. As a polar insulator, Al_2O_3 may also play an additional role in enhancing the QAH effect. It is worth noting that although all current experiments support the scenario that AlO_x likely contributes to magnetism, the microscopic mechanism remains inadequately understood owing to the challenges in directly measuring the interfacial magnetism. Further studies are required to elucidate the exact mechanisms.

In summary, we report the successful realization of the QAH effect in MnBi_2Te_4 devices capped with AlO_x by employing a revised fabrication method based on the standard EBL. By simply depositing an AlO_x layer on top of MnBi_2Te_4 , we observe a substantial enhancement of the AH effect, ultimately achieving quantization. Our experiments resolve a longstanding challenge in the field of magnetic topological materials, paving the way for fabricating high-quality devices and investigating the intricate interplay between nontrivial topology and 2D magnetism. Recently, novel transport phenomena unavailable in previous QAH systems have already been observed in 7-SL MnBi_2Te_4 with current configuration, and the enhancement of surface magnetism by AlO_x is considered crucial to explaining these new phenomena⁵⁰. This simple yet effective method is not only significant for fundamental studies, but also lays the groundwork for creating novel topological spintronic devices^{3,43,47}. It is important to note that the current exploration on utilizing AlO_x to achieve the QAH effect is still in the initial stage. More refined control of the AlO_x growth parameters^{45,46} and the interface of oxide/ MnBi_2Te_4 would further optimize the QAH effect, which remains a promising topic for future studies.

Methods

Crystal growth

High-quality MnBi_2Te_4 single crystals were synthesized by directly mixing Bi_2Te_3 and MnTe with a ratio of 1:1 in a vacuum-sealed silica ampoule. For crystal #1, the mixture was first heated up to 700 °C, and then slowly cooled down to 591 °C, followed by a long period of annealing process. The phase and crystal structure were examined by X-ray diffraction on a PANalytical Empyrean diffractometer with Cu K α radiation. For crystal #2, a small amount of Te was added to the mixture, with the ratio between Bi_2Te_3 , MnTe , and Te modified to 1:1:0.2. The ampoule was then slowly heated to 900 °C and maintained at this temperature for 1 h. Subsequently, it was cooled down to 700 °C, holding for 1 hour and then gradually cooled to 585 °C and maintained for 12 days. After the annealing, the ampoule was quenched in water to avoid phase impurities. Apart from devices #2, #4, #6, and #8, all other 13 devices were obtained from crystal #2. The four devices have already represented the samples showing the largest AH conductivity in the devices prepared from crystal #1.

Device fabrication

MnBi_2Te_4 flakes were mechanically exfoliated onto 285 nm thick SiO_2/Si substrate by using the Scotch tape method in an Ar-filled glovebox with O_2 and H_2O level lower than 0.1 ppm. Initially, the substrate was thoroughly cleaned with acetone, isopropanol, and deionized water. Then the surface of SiO_2/Si was treated with air plasma at ~ 125 Pa for 3 min. The tape-covered substrate was heated up to 60 °C for 3 min to facilitate smooth exfoliation of the single crystals into flakes. Micrometer-sized thin flakes can be obtained by mechanically exfoliation on thick flakes for several times. The thickness was identified by optical contrast measurement in the glovebox immediately after exfoliation. After the target flakes were obtained, a 3-nm aluminum was deposited onto the surface using a thermal evaporator with a deposition rate 0.04 nm/s under a vacuum better than 4×10^{-4} Pa. Oxygen was then introduced into the chamber, and the aluminum layer was oxidized for 5 min at a pressure of 2×10^{-2} Pa. For device #11, an extra deposition process with

longer time was employed to compare the influence of different AlO_x parameter on transport. During this process, an additional 30-nm AlO_x was deposited under a controlled oxygen environment at a pressure of 2×10^{-2} Pa.

To assess the effect of PMMA on the MnBi_2Te_4 samples, 270 nm thick PMMA was spin-coated onto the samples in an Ar-filled glovebox at a controlled speed of 4000 round/min. The samples were then heated at 60 °C for 7 min and left to stabilize in the glovebox for 24 h. Subsequently, the samples were then immersed in acetone for 20 min, rinsed with acetone followed by isopropanol, and their optical contrasts were measured immediately after the removal of PMMA. Standard EBL was employed on MnBi_2Te_4 samples to pattern the Hall bar structure. The oxidized aluminum was first etched from the sample surface using an Ar ion milling machine at a pressure of 2×10^{-4} Torr for 75 s. Cr/Au electrodes (3/50 nm) were then deposited using a thermal evaporator connected to a glovebox. Following this, the samples were again spin-coated with PMMA adopting the same parameters as before for further protection.

Transport measurement

Standard four probe transport measurements for devices #1 to #16 were carried out in a cryostat with the lowest T of -1.5 K and an out-of-plane magnetic field up to -8 T. The longitudinal and Hall voltages were acquired simultaneously via two lock-in amplifiers with an AC current (100 nA, 13 Hz) generated by a Keithley 6221 current source meter. For device #17, the transport was performed in a dilution refrigerator with AC current excitation of 10 nA at 13 Hz. To correct the geometrical misalignment, both the longitudinal and Hall signals were symmetrized and antisymmetrized with respect to the magnetic field. The back-gate voltage was applied by a Keithley 2400 source meter through the SiO_2/Si substrate.

MFM measurement

Cryogenic MFM experiments were conducted in a commercial atomic force microscope (atto-AFM) equipped with commercial cantilevers (spring constant $k \approx 2.8$ N/m and resonance frequency ≈ 75.8 kHz) in a closed-cycle helium cryostat. An out-of-plane magnetic field was applied using a superconducting magnet. MFM images were taken in a constant height mode with lift height of ~200 nm. The MFM signal, the change of cantilever resonance frequency, is proportional to the gradient of out-of-plane stray field. Electrostatic interaction was minimized by balancing the tip-surface potential difference.

Data availability

All data supporting the finding in the study are presented within the main text and the supplementary information. All data are available from the corresponding author upon request.

References

- He, Q. L., Hughes, T. L., Armitage, N. P., Tokura, Y. & Wang, K. L. Topological spintronics and magnetoelectronics. *Nat. Mater.* **21**, 15–23 (2022).
- Bernevig, B. A., Felser, C. & Beidenkopf, H. Progress and prospects in magnetic topological materials. *Nature* **603**, 41–51 (2022).
- Smejkal, L., Mokrousov, Y., Yan, B. H. & MacDonald, A. H. Topological antiferromagnetic spintronics. *Nat. Phys.* **14**, 242–251 (2018).
- Gong, Y. et al. Experimental realization of an intrinsic magnetic topological insulator. *Chin. Phys. Lett.* **36**, 076801 (2019).
- Li, J. et al. Intrinsic magnetic topological insulators in van der Waals layered MnBi_2Te_4 -family materials. *Sci. Adv.* **5**, eaaw5685 (2019).
- Otrokov, M. M. et al. Prediction and observation of an anti-ferromagnetic topological insulator. *Nature* **576**, 416–422 (2019).
- Lee, I. et al. Imaging Dirac-mass disorder from magnetic dopant atoms in the ferromagnetic topological insulator $\text{Cr}_x(\text{Bi}_{0.1}\text{Sb}_{0.9})_{2-x}\text{Te}_3$. *Proc. Natl. Acad. Sci. USA* **112**, 1316–1321 (2015).
- Deng, Y. et al. Quantum anomalous Hall effect in intrinsic magnetic topological insulator MnBi_2Te_4 . *Science* **367**, 895–900 (2020).
- Ge, J. et al. High-Chern-number and high-temperature quantum Hall effect without Landau levels. *Natl. Sci. Rev.* **7**, 1280–1287 (2020).
- Liu, C. et al. Robust axion insulator and Chern insulator phases in a two-dimensional antiferromagnetic topological insulator. *Nat. Mater.* **19**, 522–527 (2020).
- Gao, A. et al. Layer Hall effect in a 2D topological axion antiferromagnet. *Nature* **595**, 521–525 (2021).
- Ovchinnikov, D. et al. Intertwined topological and magnetic orders in atomically thin Chern insulator MnBi_2Te_4 . *Nano Lett.* **21**, 2544–2550 (2021).
- Cai, J. Q. et al. Electric control of a canted-antiferromagnetic Chern insulator. *Nat. Commun.* **13**, 1668 (2022).
- Yang, S. Q. et al. Odd-even layer-number effect and layer-dependent magnetic phase diagrams in MnBi_2Te_4 . *Phys. Rev. X* **11**, 011003 (2021).
- Liu, C. et al. Magnetic-field-induced robust zero Hall plateau state in MnBi_2Te_4 Chern insulator. *Nat. Commun.* **12**, 4647 (2021).
- Zhang, R.-X., Wu, F. & Sarma, S. D. Möbius insulator and higher-order topology in $\text{MnBi}_{2n}\text{Te}_{3n+1}$. *Phys. Rev. Lett.* **124**, 136407 (2020).
- Qiu, J. X. et al. Axion optical induction of antiferromagnetic order. *Nat. Mater.* **22**, 583–590 (2023).
- Gao, A. Y. et al. Quantum metric nonlinear Hall effect in a topological antiferromagnetic heterostructure. *Science* **381**, 181–186 (2023).
- Wang, N. Z. et al. Quantum-metric-induced nonlinear transport in a topological antiferromagnet. *Nature* **621**, 487 (2023).
- Zhang, S. et al. Experimental observation of the gate-controlled reversal of the anomalous Hall effect in the intrinsic magnetic topological insulator MnBi_2Te_4 device. *Nano Lett.* **20**, 709–714 (2020).
- Zhang, Z. et al. Controlled large non-reciprocal charge transport in an intrinsic magnetic topological insulator MnBi_2Te_4 . *Nat. Commun.* **13**, 6191 (2022).
- Li, Y. et al. Fabrication-induced even-odd discrepancy of magnetotransport in few-layer MnBi_2Te_4 . *Nat. Commun.* **15**, 3399 (2024).
- Sass, P. M., Kim, J., Vanderbilt, D., Yan, J. Q. & Wu, W. D. Robust A-type order and spin-flop transition on the surface of the anti-ferromagnetic topological insulator MnBi_2Te_4 . *Phys. Rev. Lett.* **125**, 037201 (2020).
- Garnica, M. et al. Native point defects and their implications for the Dirac point gap at MnBi_2Te_4 (0001). *NPJ Quantum Mater.* **7**, 7 (2022).
- Shikin, A. M. et al. Sample-dependent Dirac-point gap in MnBi_2Te_4 and its response to applied surface charge: a combined photo-emission and ab initio study. *Phys. Rev. B* **104**, 115168 (2021).
- Liu, Y. H. et al. Site mixing for engineering magnetic topological insulators. *Phys. Rev. X* **11**, 021033 (2021).
- Huang, Z., Du, M.-H., Yan, J. & Wu, W. Native defects in anti-ferromagnetic topological insulator MnBi_2Te_4 . *Phys. Rev. Mater.* **4**, 121202 (2020).
- Mazza, A. R. et al. Surface-driven evolution of the anomalous Hall effect in magnetic topological insulator MnBi_2Te_4 thin films. *Adv. Funct. Mater.* **32**, 2202234 (2022).
- Li, H. et al. Dirac surface states in intrinsic magnetic topological insulators EuSn_2As_2 and $\text{MnBi}_{2n}\text{Te}_{3n+1}$. *Phys. Rev. X* **9**, 041039 (2019).
- Tan, H. & Yan, B. Distinct magnetic gaps between antiferromagnetic and ferromagnetic orders driven by surface defects in the topological magnet MnBi_2Te_4 . *Phys. Rev. Lett.* **130**, 126702 (2023).
- Hao, Y. J. et al. Gapless surface dirac cone in anti-ferromagnetic topological insulator MnBi_2Te_4 . *Phys. Rev. X* **9**, 041038 (2019).
- Li, B. et al. Quasi-two-dimensional ferromagnetism and anisotropic interlayer couplings in the magnetic topological insulator MnBi_2Te_4 . *Phys. Rev. B* **104**, L220402 (2021).
- Li, Q. et al. Imaging the breakdown and restoration of topological protection in magnetic topological insulator MnBi_2Te_4 . *Adv. Mater.* **36**, 2312004 (2024).

34. Wang, D. H., Wang, H. Q., Xing, D. Y. & Zhang, H. J. Three-Dirac-fermion approach to unexpected universal gapless surface states in van der Waals magnetic topological insulators. *Sci. China Phys. Mech.* **66**, 297211 (2023).
35. Hou, F. C. et al. Te-vacancy-induced surface collapse and reconstruction in antiferromagnetic topological insulator MnBi₂Te₄. *ACS Nano* **14**, 11262–11272 (2020).
36. Bai, Y. et al. Quantized anomalous Hall resistivity achieved in molecular beam epitaxy-grown MnBi₂Te₄ thin films. *Natl. Sci. Rev.* **11**, nwad189 (2023).
37. Nagaosa, N., Sinova, J., Onoda, S., MacDonald, A. H. & Ong, N. P. Anomalous Hall effect. *Rev. Mod. Phys.* **82**, 1539–1592 (2010).
38. Yu, R. et al. Quantized anomalous Hall effect in magnetic topological insulators. *Science* **329**, 61–64 (2010).
39. Zhang, D. M. et al. Interplay between ferromagnetism, surface states, and quantum corrections in a magnetically doped topological insulator. *Phys. Rev. B* **86**, 205127 (2012).
40. Checkelsky, J. G., Ye, J. T., Onose, Y., Iwasa, Y. & Tokura, Y. Dirac-fermion-mediated ferromagnetism in a topological insulator. *Nat. Phys.* **8**, 729–733 (2012).
41. Chang, C. Z. et al. Thin films of magnetically doped topological insulator with carrier-independent long-range ferromagnetic order. *Adv. Mater.* **25**, 1065–1070 (2013).
42. Ding, L. et al. Crystal and magnetic structures of magnetic topological insulators MnBi₂Te₄ and MnBi₄Te₇. *Phys. Rev. B* **101**, 020412(R) (2020).
43. Hellman, F. et al. Interface-induced phenomena in magnetism. *Rev. Mod. Phys.* **89**, 025006 (2017).
44. Cuellar, F. A. et al. Reversible electric-field control of magnetization at oxide interfaces. *Nat. Commun.* **5**, 4215 (2014).
45. Rodmacq, B., Auffret, S., Dieny, B., Monso, S. & Boyer, P. Crossovers from in-plane to perpendicular anisotropy in magnetic tunnel junctions as a function of the barrier degree of oxidation. *J. Appl. Phys.* **93**, 7513–7515 (2003).
46. Monso, S. et al. Crossover from in-plane to perpendicular anisotropy in Pt/CoFe/AlO_x sandwiches as a function of Al oxidation: a very accurate control of the oxidation of tunnel barriers. *Appl. Phys. Lett.* **80**, 4157–4159 (2002).
47. Dieny, B. & Chshiev, M. Perpendicular magnetic anisotropy at transition metal/oxide interfaces and applications. *Rev. Mod. Phys.* **89**, 025008 (2017).
48. Li, Y., Jiang, Z., Li, J., Xu, S. & Duan, W. Magnetic anisotropy of the two-dimensional ferromagnetic insulator MnBi₂Te₄. *Phys. Rev. B* **100**, 134438 (2019).
49. Coey, J. M. D. *Magnetism and Magnetic Materials* (Cambridge University Press, 2010).
50. Lian, Z. et al. Antiferromagnetic quantum anomalous Hall effect modulated by spin flips and flops. Preprint at <http://arxiv.org/abs/2405.08686> (2024).

Acknowledgements

The authors appreciate the assistance provided by Prof. Yang Wu and Dr. Hao Li during the MnBi₂Te₄ crystal growth. Chang Liu was sponsored by National Natural Science Foundation of China (Grant No. 12274453), Beijing Nova Program (Grant No. 20240484574), and Open Research Fund Program of the State Key Laboratory of Low-Dimensional Quantum Physics (Grant No. KF202204). Jinsong Zhang was supported by

National Natural Science Foundation of China (Grants Nos. 12274252 and 12350404). Yayu Wang was supported by the Basic Science Center Project of Natural Science Foundation of China (Grant No. 52388201) and the New Cornerstone Science Foundation through the New Cornerstone Investigator Program and the XPLORER PRIZE. Yayu Wang, Jinsong Zhang, and Chang Liu acknowledge the support from Innovation Program for Quantum Science and Technology (Grant No. 2021ZD0302502). Wenbo Wang was sponsored by National Key Research and Development Program of China (Grant No. 2022YFA1403000), and National Natural Science Foundation of China (Grant No. 12374161).

Author contributions

C.L. conceived the project. C.L., Y.Y.W., J.S.Z., W.J.J., and W.B.W. supervised the research. Y.C.W. grew the MnBi₂Te₄ crystals, Y.Q.W., B.H.F., Z.C.L., and S.Y. fabricated the devices and performed the transport measurements with the help of Y.C.W., Y.X.L., L.C.X., and Z.T.G. X.T.Y. and W.B.W. performed the MFM measurements. C.L. and Y.Q.W. prepared the manuscript with comments from all authors.

Competing interests

The authors declare no competing interests.

Additional information

Supplementary information The online version contains supplementary material available at <https://doi.org/10.1038/s41467-025-57039-7>.

Correspondence and requests for materials should be addressed to Chang Liu.

Peer review information *Nature Communications* thanks Yonglong Xie, and the other, anonymous, reviewer(s) for their contribution to the peer review of this work. A peer review file is available.

Reprints and permissions information is available at <http://www.nature.com/reprints>

Publisher's note Springer Nature remains neutral with regard to jurisdictional claims in published maps and institutional affiliations.

Open Access This article is licensed under a Creative Commons Attribution 4.0 International License, which permits use, sharing, adaptation, distribution and reproduction in any medium or format, as long as you give appropriate credit to the original author(s) and the source, provide a link to the Creative Commons licence, and indicate if changes were made. The images or other third party material in this article are included in the article's Creative Commons licence, unless indicated otherwise in a credit line to the material. If material is not included in the article's Creative Commons licence and your intended use is not permitted by statutory regulation or exceeds the permitted use, you will need to obtain permission directly from the copyright holder. To view a copy of this licence, visit <http://creativecommons.org/licenses/by/4.0/>.

© The Author(s) 2025